

Nianfeng WANG, Bicheng CHEN, Xiandong GE, Xianmin ZHANG, Wenbin WANG

Modular crawling robots using soft pneumatic actuators

© The Author(s) 2021. This article is published with open access at link.springer.com and journal.hep.com.cn

Abstract Crawling robots have elicited much attention in recent years due to their stable and efficient locomotion. In this work, several crawling robots are developed using two types of soft pneumatic actuators (SPAs), namely, an axial elongation SPA and a dual bending SPA. By constraining the deformation of the elastomeric chamber, the SPAs realize their prescribed motions, and the deformations subjected to pressures are characterized with numerical models. Experiments are performed for verification, and the results show good agreement. The SPAs are fabricated by casting and developed into crawling robots with 3D-printing connectors. Control schemes are presented, and crawling tests are performed. The speeds predicted by the numerical models agree well with the speeds in the experiments.

Keywords soft robot, soft pneumatic actuator, kinematic model, crawling robot, modular design

1 Introduction

Soft robots have elicited much attention in recent years because they offer a promising means of interaction due to their flexibility and adaptivity. The emergence of soft robots has stimulated developments in soft actuation technologies, such as electroactive [1–6], magnetoactive [7–10], and pneumatic [11–15] actuators. Pneumatic actuators are popular because they are cheap, lightweight, powerful, highly customizable, and easily fabricated

[16,17]. They have been used in many applications, including manipulators [18,19], rehabilitation devices [20–22], and locomotion robots [23,24].

Made with silicone materials, soft pneumatic actuators (SPAs) can respond to air pressure with large deformation because of their inherent softness. The performance of SPAs can be affected by chamber layouts and the integration of reinforcements [25–27]. Many previous studies have reported that SPAs with different configurations achieve different types of actuations under pressure. Connolly et al. [28] proposed several fiber-reinforced SPAs that can realize expansion, extension, and twisting at specific fiber angles. Gorissen et al. [29] designed a flexible SPA for tilting micromirrors that can twist by planning the chamber arrays. Mosadegh et al. [30] presented a novel SPA with a network of small channels to achieve rapid bending.

However, designers cannot easily achieve their desired motions due to the long development time and high costs. A modular design approach can be used to solve this problem. In this approach, each basic actuation can be realized by a specific module, and integrated motions can be completed by modules working cooperatively. Although proposals to make rigid robots universal and flexible have been presented, modular design is still commonly used in the design of soft robots that can perform designated tasks, such as creeping, crawling, jumping, and gripping [31–33].

Crawling robots have elicited extensive attention due to their high speed and good locomotion stability. Crawling robots are generally bio-inspired and can move like a worm with several different gaits actuated in sequence. Many crawling robots have been proposed in previous studies. Shepherd et al. [24] presented an integrated multi-gait robot with five bending SPAs working together to realize crawling. Jiao et al. [34] designed a modular robot using seven vacuum-powered twisting SPAs to crawl with different gaits. Ning et al. [35] introduced an inchworm-inspired robot with a multi-segment SPA that can crawl using the friction hysteresis effect.

These studies focused on the design of crawling robots by using different techniques to improve performance in

Received April 14, 2020; accepted August 11, 2020

Nianfeng WANG (✉), Bicheng CHEN, Xiandong GE, Xianmin ZHANG
Guangdong Key Laboratory of Precision Equipment and Manufacturing Technology, School of Mechanical and Automotive Engineering, South China University of Technology, Guangzhou 510640, China
E-mail: menfwang@scut.edu.cn

Wenbin WANG (✉)
School of Mechanical and Electrical Engineering, Shenzhen Polytechnic, Shenzhen 518055, China
E-mail: wangwenbin@szept.edu.cn

experiments. However, the motions of crawling robots were not analyzed based on the deformations of modules, which makes programmable motions difficult. Moreover, crawling robots are usually bio-inspired and do not consider module assembly. This study proposes several soft modular robots that can move straight and turn around on a plane by utilizing the two-anchor crawling mode [36]. Two types of SPAs, namely, an axial-elongation SPA (aeSPA) and a dual-bending SPA (dbSPA), are used to design the soft robots. Numerical models are built to characterize the relationship between deformations and pressures on the basis of the principle of virtual work. This work also pays attention to the layouts of crawling robots by comparing the performance of several robots through tests that involve straight crawling and turning.

The rest of the paper is organized as follows. Section 2 presents the concept of crawling robots with the constructed modular SPAs. Section 3 introduces the numerical models for determining the deformations of SPAs under pressures on the basis of the principle of virtual work. The modules built using SPAs and connectors are tested in Section 4. Experiments are conducted in Section 5 to test different crawling robots. The control schemes are illustrated, and the crawling speeds are recorded. The last section presents the conclusions and discussions.

2 Prototype design of modular crawling soft pneumatic robots

The global motion of crawling robots can be divided into two types of modules, namely, elongation and bending, which make up the modules of the kinetostatic code. Figure 1 illustrates the concept of a crawling robot. The robot can be simply divided into front, central, and rear segments, as shown Fig. 1(a). The two-anchor crawling mode is adopted. Specifically, the front and rear segments take turns in anchoring the robot to the ground, and the central segment is used to provide extending and bending deformations. By actuating different segments in a

sequence, the crawling robot can move smoothly on the ground. Figures 1(b) and 1(c) show the straight crawling and turning motions of the crawling robot.

For the design of a modular crawling soft robot, two kinds of SPAs, namely, aeSPA and dbSPA, are introduced as shown in Fig. 2. The aeSPA is made of an elastomeric matrix with one chamber, and dbSPA consists of an elastomeric matrix with two chambers. Rigid rings are used outside to restrict the radial expansion of the SPAs and obtain the desired deformation. The aeSPA extends under pressure, and dbSPA can not only bend with one chamber pressurized but also extend with two chambers under pressure.

Figure 3 shows several modules that are used in soft crawling robots, including long aeSPA for elongation, short aeSPA for anchoring, dbSPA for elongation and bending, segment connector, and module connector. The short aeSPA is utilized as an anchor that will crush on the ground under pressure to increase the friction force. The long aeSPA and dbSPA are similar in appearance, but a black ring is used in aeSPA (50 mm) for distinction. For illustration, several symbols are utilized for these modules.

Several crawling robots are obtained by assembling these modules in different morphologies, as shown in Fig. 4. The obtained soft robots are labeled as b-db-SR, b-db2-SR, b-db-ae-SR, q-db-SR, q-db2-SR, q-db-ae-SR, and q-ae2-SR. The names of these robots are the abbreviations of the types and modules used. The b-db-SR refers to a biped crawling soft robot with one dbSPA as the central segment. The b-db2-SR refers to a biped crawling soft robot with two series dbSPAs as the central segment. The b-db-ae-SR refers to a biped crawling soft robot with one dbSPA and one aeSPA in series as the central segment. The q-db-SR refers to a quadruped crawling soft robot with one dbSPA as the central segment. The q-db2-SR refers to a quadruped crawling soft robot with two series dbSPAs as the central segment. The q-db-ae-SR refers to a quadruped crawling soft robot with one dbSPA and one aeSPA in series as the central segment, and q-ae2-SR refers to a quadruped crawling soft robot with two parallel aeSPAs as

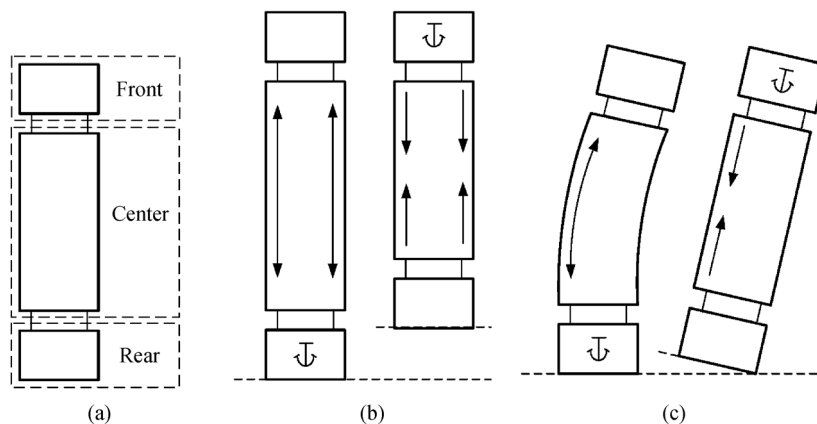


Fig. 1 Concept of a crawling robot: (a) Crawling robot with three segments, (b) diagram of straight crawling, and (c) diagram of turning.

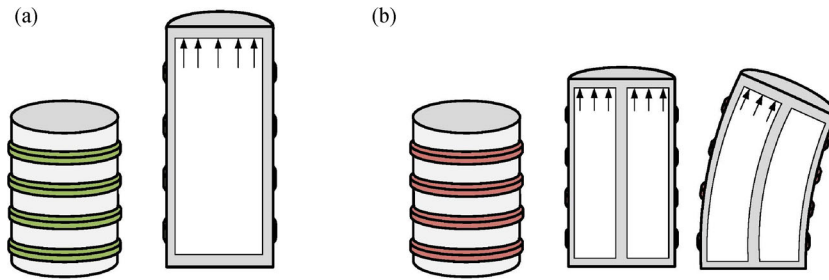


Fig. 2 Configuration and deformation of SPAs: (a) aeSPA and (b) dbSPA.

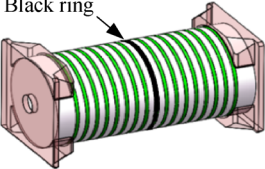

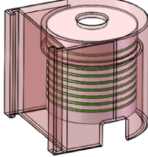

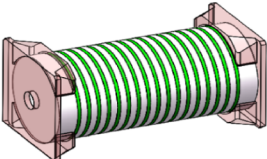
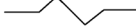
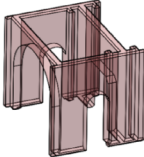

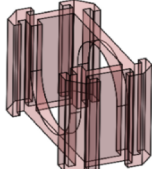

Module	Model	Symbol
Long aeSPA		
Short aeSPA		
dbSPA		
Segment connector		
Module connector		

Fig. 3 Modules of soft crawling robots.

the central segment. These robots consist of front, central, and rear segments and can mimic the locomotion behavior of earthworms. The front and rear segments take turns in anchoring to the ground, and simultaneously, the central segment extends or bends to achieve the desired motion. Biped robots demonstrate sufficient flexibility for narrow spaces, and quadruped robots are more stable for crawling. The deformations of aeSPA and dbSPA under pressure are

investigated in the next section to characterize the crawling motion of these robots.

3 Characteristics of SPAs

The construction of aeSPA and dbSPA, which includes an elastomer matrix, several rigid rings, and two rigid plates,

Type	Name	Diagram	Robot
Biped robot	b-db-SR		
	b-db2-SR		
	b-db-ae-SR		
Quadruped robot	q-db-SR		
	q-db2-SR		
	q-db-ae-SR		
	q-ae2-SR		

Fig. 4 Assembled soft crawling robots.

is shown in Fig. 5. The elastomeric matrix for aeSPA has one chamber, and the elastomeric matrix for dbSPA has two matrices. The rigid rings are fixed on the external surface of the elastomeric matrix with the help of the narrow gaps. The depth and width of a gap are 0.5 and 1 mm, respectively. A thick wall is used for the elastomeric matrix in consideration of airtightness and to avoid matrix fracture. In this manner, the materials between adjacent gaps on the surface of the elastomeric matrix can be ignored. Two rigid plates are attached to the sides of the elastomeric matrix to restrict the swelling and radial expansion of the end surfaces so that the compressions of the two sides of the elastomeric matrix can be disregarded. That is, the deformations of the SPAs are only related to the elastomeric matrix and not to the top walls, bottom walls, and wrinkles.

3.1 Modeling for aeSPA

Figure 6 shows the cross sections of aeSPA in the initial state without pressure and in the deformed state under pressure. The dimensions of aeSPA in the initial state are described by height h_a , radius r_a , and thickness t_a , which change into height \bar{h}_a , radius \bar{r}_a , and thickness \bar{t}_a in the deformed state. The extension of aeSPA is the height between h_a and \bar{h}_a and is referred to as Δh_a .

The aeSPA is assumed to extend uniformly under pressure. Hence, the stretches in three directions can be obtained as $\lambda_{a1} = \bar{h}_a/h_a$, $\lambda_{a2} = 2\pi\bar{r}_a/(2\pi r_a) = \bar{r}_a/r_a$, and $\lambda_{a3} = \bar{t}_a/t_a$. Given that the elastomer is considered incompressible, the volume remains constant in both states as follows:

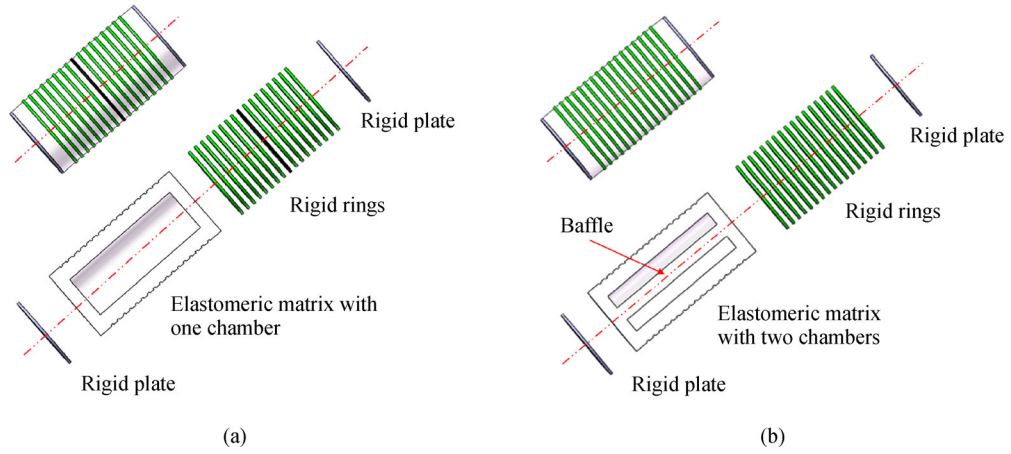


Fig. 5 Construction of SPAs: (a) aeSPA and (b) dbSPA.

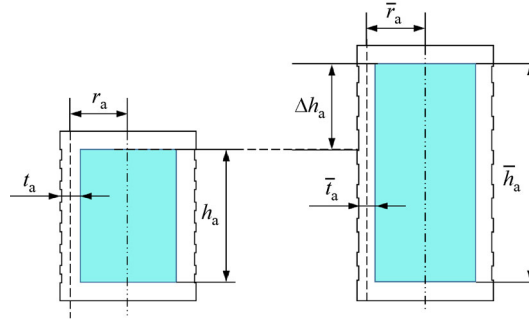


Fig. 6 Model of aeSPA before and after actuation.

$$\begin{aligned} \bar{V}_{am} &= \pi \left(\left(\bar{r}_a + \frac{\bar{t}_a}{2} \right)^2 - \left(\bar{r}_a - \frac{\bar{t}_a}{2} \right)^2 \right) \bar{h}_a \\ &= \pi \left(\left(r_a + \frac{t_a}{2} \right)^2 - \left(r_a - \frac{t_a}{2} \right)^2 \right) h_a = V_{am}, \end{aligned} \quad (1)$$

where V_{am} is the volume of the elastomeric wall in the initial state and \bar{V}_{am} is the volume in the deformed state. Considering that aeSPA is restricted by the rigid rings outside, the external radius is constant so that $\bar{r}_a + \bar{t}_a/2 = r_a + t_a/2$. Thus, \bar{r}_a and \bar{t}_a can be expressed by \bar{h}_a using the equation above, and the stretches can be rewritten as

$$\left\{ \begin{aligned} \lambda_{a1} &= \frac{\bar{h}_a}{h_a}, \\ \lambda_{a2} &= \frac{2r_a\bar{h}_a + t_a\bar{h}_a + \sqrt{\bar{h}_a(4r_a^2\bar{h}_a + t_a^2\bar{h}_a - 8h_a r_a t_a + 4r_a t_a \bar{h}_a)}}{4r_a\bar{h}_a}, \\ \lambda_{a3} &= \frac{2r_a\bar{h}_a + t_a\bar{h}_a - \sqrt{\bar{h}_a(4r_a^2\bar{h}_a + t_a^2\bar{h}_a - 8h_a r_a t_a + 4r_a t_a \bar{h}_a)}}{2t_a\bar{h}_a}. \end{aligned} \right. \quad (2)$$

In other words, the deformation of aeSPA can be determined directly by \bar{h}_a . For an arbitrary system variation, the gain in strain energy is equal to the positive work done by pressure as follows:

$$\left\{ \begin{aligned} p\delta V_{ap} &= V_{am}\delta W_a, \\ V_{ap} &= \pi \left(\bar{r}_a - \frac{\bar{t}_a}{2} \right)^2 \bar{h}_a, \end{aligned} \right. \quad (3)$$

where p is pressure, V_{ap} is the volume of the chamber, and W_a is the hyper-elastic strain energy density function. The Yeoh model is used in this study, and it can be expressed as

$$W = \sum_{i=1}^N C_{i0}(\lambda_1^2 + \lambda_2^2 + \lambda_3^2 - 3)^i, \quad (4)$$

where C_{i0} ($i = 1, 2, \dots, N$) are the coefficients of the material and λ_1, λ_2 , and λ_3 are the main stretch ratios in three directions. With the equation above, the relationship between pressure p and deformation Δh_a of aeSPA can be easily obtained.

3.2 Modeling for dbSPA

The extending deformation of dbSPA can be derived by referring to that of aeSPA but with an internal baffle of the chamber, which restricts the elongation by reducing the work of pressure and increasing the hyper-elastic strain energy. The situation is different for bending dbSPA. For enhanced understanding, the procedure of bending deformation is assumed to proceed via two virtual steps, as shown in Fig. 7, with initial height h_b , radius r_b , and thickness t_b . In the first step, the left chamber extends under pressure, and the right chamber remains unchanged. The dimension of the left part of dbSPA is described by height \bar{h}_b , radius \bar{r}_b , thickness \bar{t}_b , and extension Δh_b . In the second step, dbSPA starts to bend to the right to make the height of the internal baffle continuous, and the bending angle is denoted as ϕ .

To obtain bending angle ϕ , dbSPA is assumed to bend uniformly under pressure and discretized into n units sliced by the horizontal plane, as shown in Fig. 8. Each unit with a dimension of height h_b/n bends under pressure and obtains a bending angle of $\alpha = \phi/n$. The generatrix on the right is assumed to be equal to the initial value, and the generatrix on the left is assumed to be extended freely so that \bar{h}_b can be evaluated by Eq. (3). Arc $BC = \Delta h_b/(2n)$, and length $AB = 2r_b + t_b$ because the external radius is restricted by the rigid rings. Thus, the bending angle can be simply calculated in triangle ABC as

$$\beta = \frac{\alpha}{2} = \arctan \frac{BC}{AB} = \arctan \frac{\Delta h_b}{2n(2r_b + t_b)}. \quad (5)$$

With β as the small angle with sufficiently large units n , bending angle ϕ can be simply calculated as

$$\phi = 2n\beta = n\alpha = \frac{k\Delta h_b}{2r_b + t_b}, \quad (6)$$

where k is introduced as an adjunctive parameter to fit the experimental results ($k = 1.46$ in this work). Angle ϕ is constant for any sufficiently large segments n , and it is related to the extension and external diameter of SPAs.

4 Evaluations of SPAs

The casting method is adopted to make the SPAs, and the fabrication processes are shown in Fig. 9. The processes use silicone rubber (Ecoflex 00-50, Smooth-On, Inc., USA) and 3D-printed molds. Four corner blocks and an inner core are assembled to form a mold. The silicone solution is poured into the mold, and an elastomeric matrix is obtained after solidification for 3 h. In this process, the silicone solution should be added continuously to avoid shrinkages and bubbles. For aeSPA, the end surfaces of the elastomeric matrix are sealed with a lid made of silicone solution. For dbSPA, the elastomeric matrix is placed on a core to form one end face and the inner baffle. Then, another end face of the elastomeric matrix is sealed with a lid made of silicone solution. The rigid rings are placed outside of the elastomeric matrix one by one and fixed on the surface of the elastomeric matrix with the wrinkles. The elastomeric matrix is then drilled to make holes, and the air tubes are glued with silicone. Several SPA modules are fabricated through this process. The thickness and radius of the SPAs are 6 and 12 mm, respectively. The length of the short aeSPA is 25 mm, and the length of the long aeSPA and dbSPA is 50 mm.

Figure 10 shows the platform for the SPA experiments, where a compressor is used to supply air and a reducing valve with a digital barometer is utilized to control the

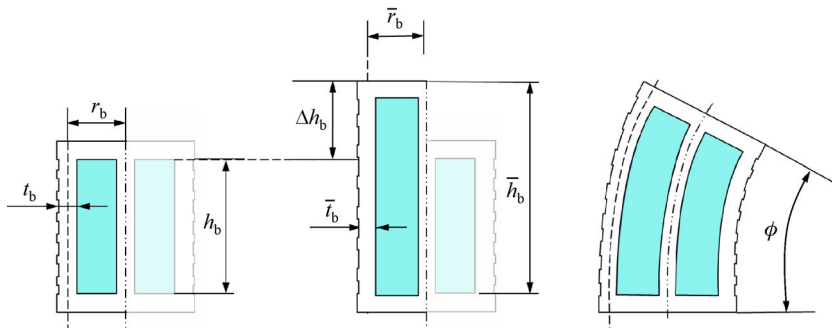


Fig. 7 Model of dbSPA before actuation, and the virtual and real deformation of the bending dbSPA.

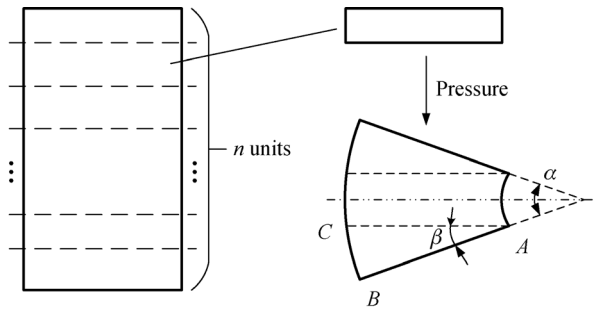


Fig. 8 Discretization of dbSPA and bending deformation of a unit with pressure.

pressures. The extensions of aeSPA and dbSPA are detected using a laser displacement sensor (IL-030, Keyence Co., Ltd., Japan), and the bending angle of dbSPA is extracted from an image obtained by a camera. The applied pressure is from 2 to 30 kPa, with a step of 2 kPa, and measurements are performed in the static state. The static state in this work refers to the period when the change in SPA displacement is less than 0.1 mm or 1° within 10 s.

Figure 11 shows the deformations of aeSPA and dbSPA and the comparison of numerical and experimental results. The extension and rotation angle increase with pressure, and the slope of the curve becomes steep. Similar results are obtained from the numerical models and experiments, indicating the effectiveness of the numerical model. The extension of the long aeSPA (50 mm) is about twice as much as that of the short aeSPA (25 mm) and dbSPA. The extension of dbSPA is much smaller than that of the long aeSPA because of the inner baffle.

Applying quasi-static numerical models is impractical because these models require so much actuation time. In consideration of practicability, the times before the static state are used for practical application. In this manner, the quasi-static model can be converted to a dynamic one.

Figure 12 shows the inflation and deflation times of different segments with pressures of 10, 20, and 30 kPa. The response speeds vary for different SPAs under different pressures. The larger the pressure is, the longer the inflation and deflation times are. Moreover, the inner baffle makes dbSPA deflate quickly in comparison with the long aeSPA.

5 Locomotion experiment on modular crawling soft pneumatic robots

Figure 13(a) shows the experimental setup for crawling robots. An electro-pneumatic regulator is used instead of a manual reducing valve because the former can produce pressure that is proportional to the control signal. For simplicity, the same pressures are applied in the same segments so that three electro-pneumatic regulators are enough to control the pressures from 0 to 30 kPa supplied by the compressor. The control signals for electro-pneumatic regulation are supplied by a USB data acquisition card (USB2651, Smacq Technologies Co., Ltd., China) through the LABVIEW program. Another electro-pneumatic regulator is needed to control the two chambers of dbSPA separately. The simplest control scheme is to inflate or deflate one segment in a single step, such that a complete actuation period is composed of six steps. However, several segments are actuated together to make the locomotion smooth, and the times overlap. Hence, four steps are needed, as shown in Fig. 13(b), and they are as follows:

- T₁: The central and front segments are inflated;
- T₂: The rear segment is deflated;
- T₃: The central segment is deflated and the rear segment is inflated;
- T₄: The front segment is deflated.

Notably, the rear and front segments should work separately to prevent the robots from sliding. In every step,

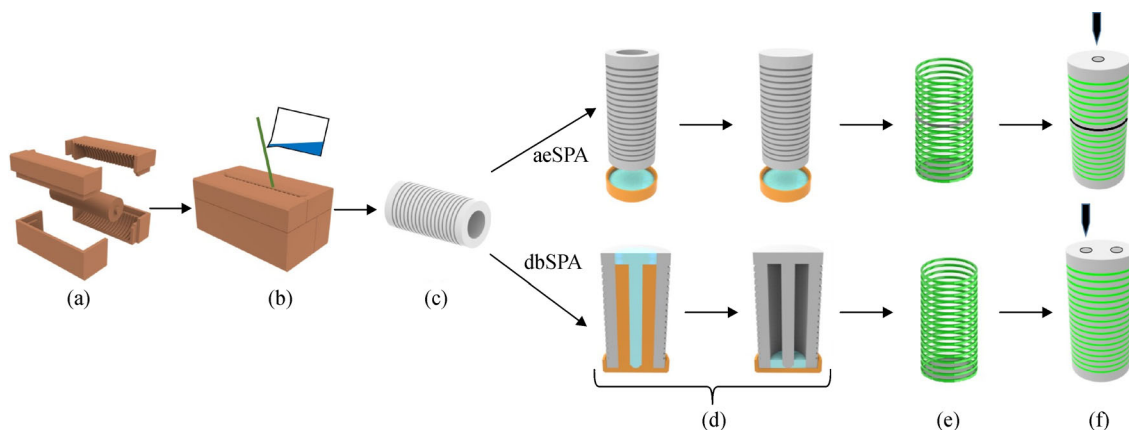


Fig. 9 Fabrication of aeSPA and dbSPA: (a) Assembly of the mold, (b) casting, (c) de-molding, (d) sealing of the wall, (e) constraining the SPA, and (f) drilling holes for the air tube.

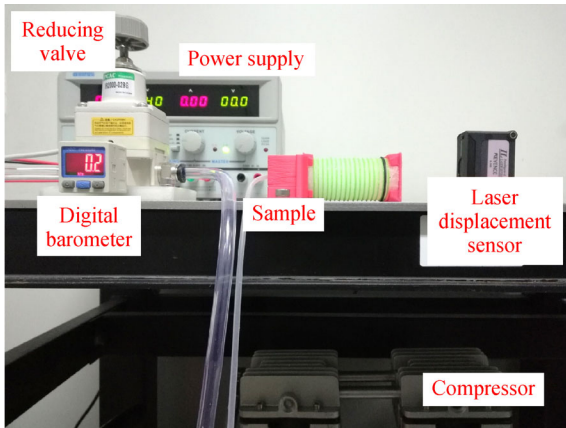


Fig. 10 Experimental setup for the tests on SPAs.

the time is determined by the maximum value of the inflation and deflation times of the SPAs with different pressures. In this manner, the total time cost in a period can be calculated for different crawling robots. The velocities of the crawling robots also can be determined because the relative actuation displacements can be obtained with the proposed numerical models.

Figure 14 shows the straight crawling and turning of b-db-SR as an example. Similar movements can be obtained with the other proposed crawling robots. Tests are conducted on straight crawling and turning to evaluate the performance of the different crawling robots.

Figure 15 shows the time of each step in the tests on the

straight crawling of robots. The actuation times of straight crawling for all the robots are about 1.6 s at pressures of 10 and 20 kPa. The actuation times of straight crawling for b-db-ae-SR, q-db-ae-SR, and q-ae2-SR are much longer than those for the other robots at a pressure of 30 kPa because of the long deflation time of aeSPA. However, given that the deformation of aeSPA is much better than that of dbSPA, these crawling robots are still promising.

In the test on straight crawling, each robot crawls a distance of 500 mm. The velocity is calculated, and the time is recorded. Figure 16 shows the results of straight crawling. The predicted velocities are evaluated by the numerical model and the given time. Among the robots with two SPAs in series as the central segment, q-db2-SR is the fastest, followed by b-db2-SR, b-db-ae-SR, and q-db-ae-SR. Among the robots with one or two SPAs in parallel as the central segment, q-ae2-SR is the fastest. In terms of the ratio of velocity to body length, q-ae2-SR is the best. In general, the performance of the quadruped robots is slightly better than that of the biped robots when the same central segments are used; the difference becomes increasingly obvious when the length of the body increases. This condition may be due to the small force of biped robots when they grip the ground. The measured velocities are lower than the predicted ones, with the errors being lower than 10%. This phenomenon may be caused by the friction of weight during crawling.

Figure 17 shows the time of each step in the tests on the turning of robots. The actuation times of turning for all the

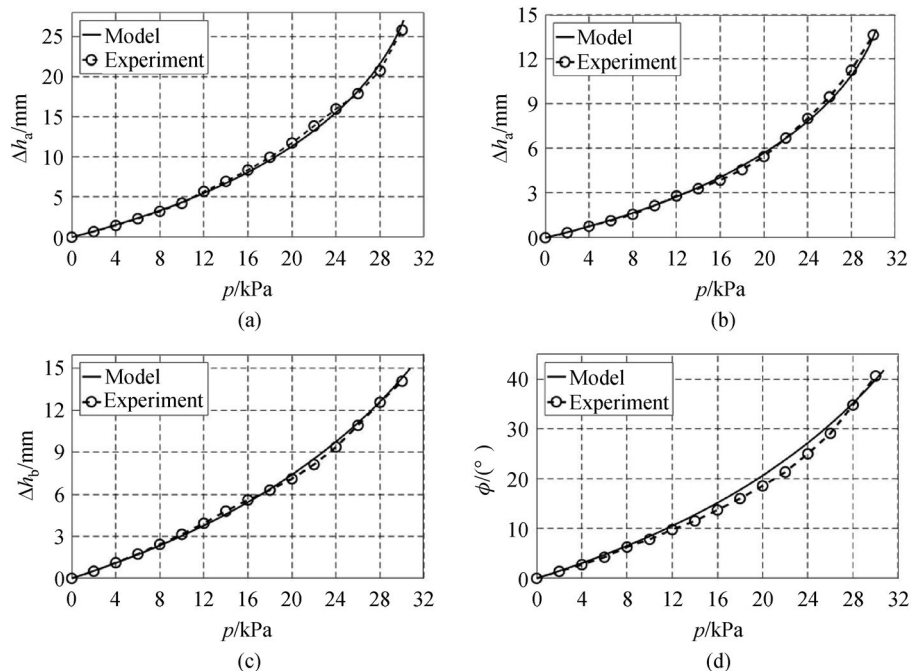


Fig. 11 Experimental and numerical results of different SPAs. (a) aeSPA (50 mm); (b) aeSPA (25 mm); (c) dbSPA (extending); (d) dbSPA (bending).

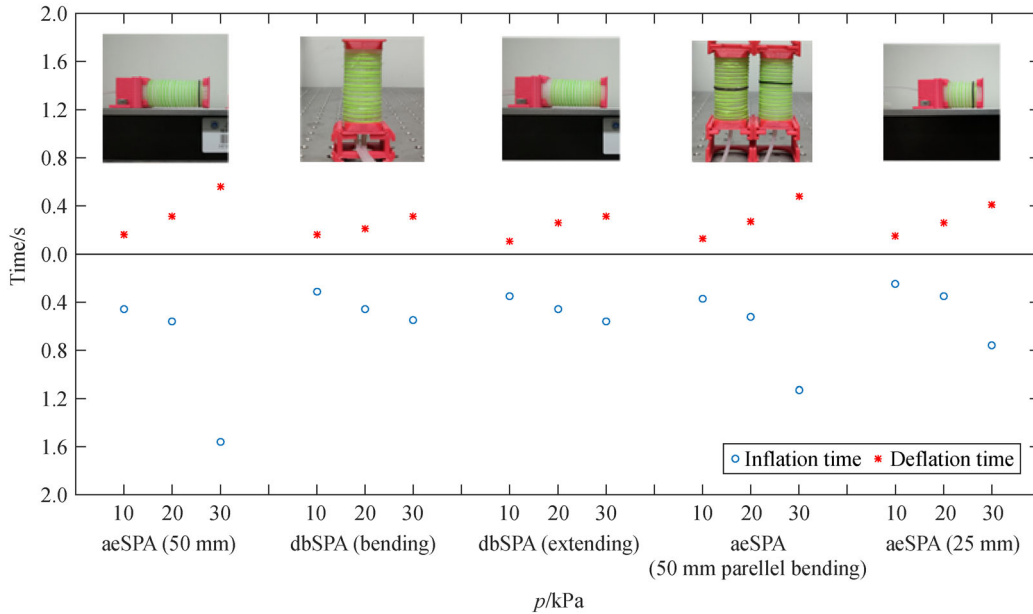


Fig. 12 Actuation times of SPAs at different pressures.

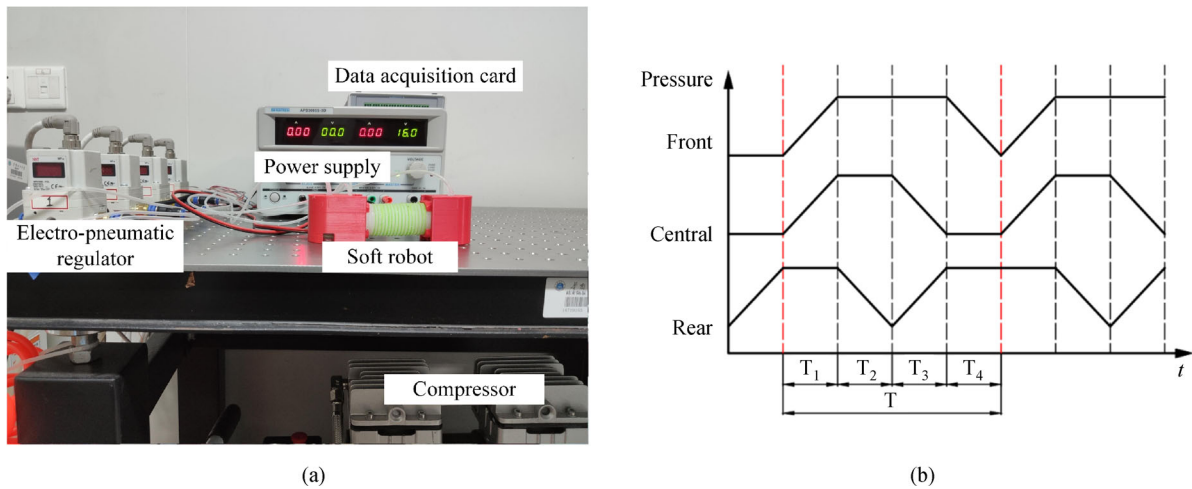


Fig. 13 Crawling tests on a soft robot: (a) Experimental setup and (b) control scheme.

robots are about 1.6 s at pressures of 10 and 20 kPa. The actuation times of turning for q-ae2-SR are much longer than those for the other robots at a pressure of 30 kPa because of the long deflation time of aeSPAs when bending in parallel.

In the test on turning motion, each robot crawls 10 periods and the velocity can be calculated with the total angle measured. Figure 18 shows the results on turning. The predicted angular velocities are evaluated by the numerical model and the given time. Among the robots with two dbSPAs in series as the central segment, b-db2-SR is slightly better than q-db2-SR. Among the robots with one dbSPA or two aeSPAs in parallel as the

central segment, b-db-SR and q-db-SR are the best. In terms of the ratio of velocity to body length, b-db-SR is the best. In general, the performance of the biped robots is better than that of the quadruped robots when the same central segments are used; the difference becomes increasingly obvious when the length of the body increases. This condition may be due to the small output force of bending of the quadruped robots. The measured angular velocities are lower than the predicted angular velocities. This phenomenon may be caused by the friction of weight during crawling. The errors of the soft robots, except for q-ae2-SR, are larger than 10%, which means the output forces of turning are inadequate.

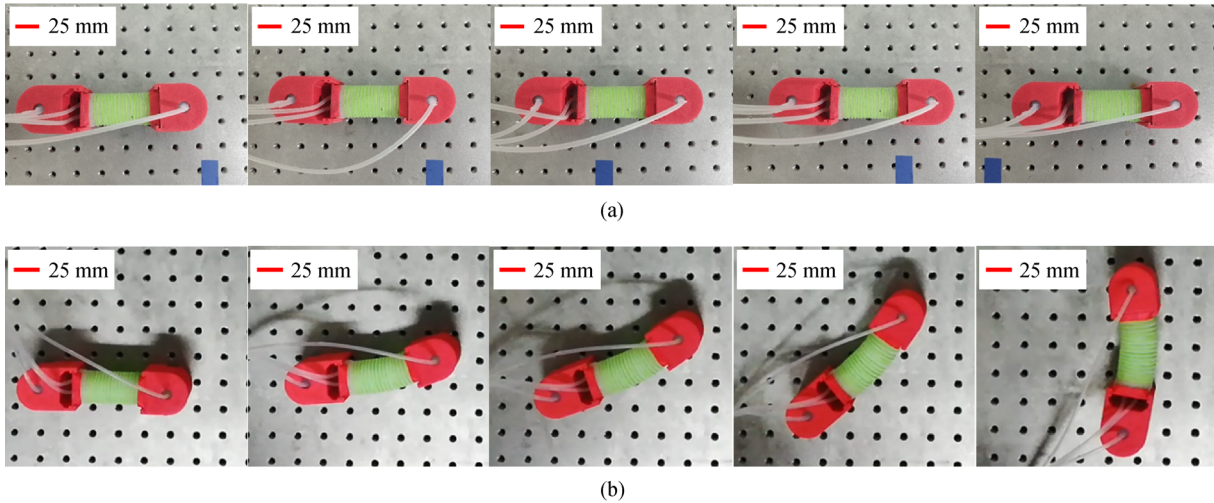


Fig. 14 Crawling process of a soft robot: (a) Straight crawling and (b) turning.

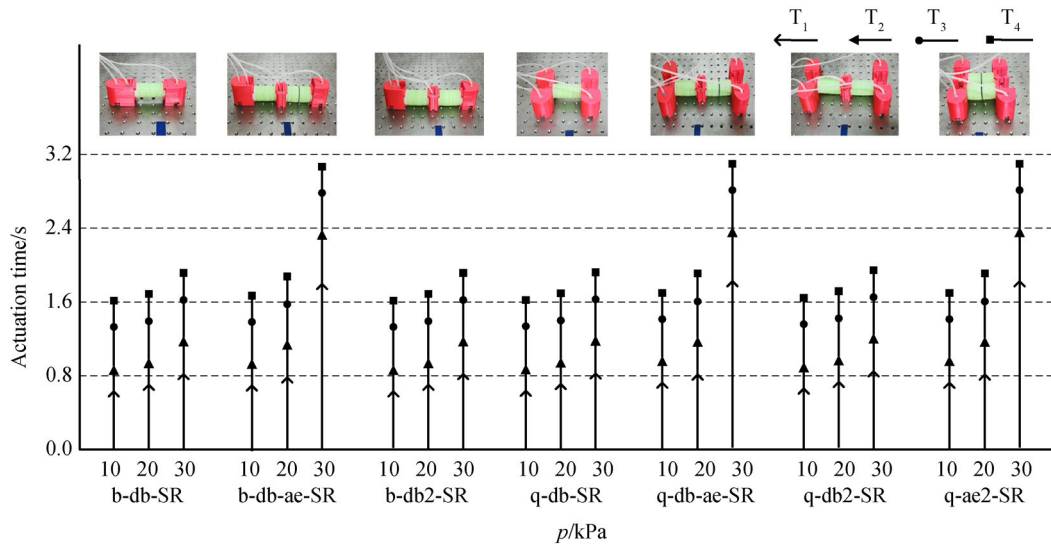


Fig. 15 Actuation time of straight crawling for the different soft robots.

6 Conclusions and future work

In this work, several worm-like soft robots that can crawl and turn are developed using SPAs. Inspired by the concept of modular design, the robots are constructed with two types of basic SPAs, namely, aeSPA and dbSPA. The aeSPA can extend under pressure, and dbSPA can bend under pressure. Numerical models of aeSPA and dbSPA are built based on the principle of virtual work to investigate the relationship between deformation and pressure. The results show good agreement with the experiment outcomes. After determining the times of the control schemes in a period, tests are conducted on the straight crawling and turning of the soft robots. Experiments show that the robots can crawl smoothly but with an

error of about 10% for straight crawling and 20% for turning. These errors may be caused by the friction of weight during crawling. In terms of the ratio of velocity to body length, q-ae2-SR is the fastest among the robots in the test on straight crawling, and b-db-SR is the best in the test on turning.

Numerical models are developed for the two types of SPAs, and the performance of different soft robots assembled with the SPAs and 3D-printed connectors is investigated. The results show that the modular design method makes it easy for soft robots to achieve straight crawling and turning. Although the numerical results of SPAs are in accordance with the experiment outcomes, the soft robot systems do not work well because of the friction of weight; a similar systematic error is obtained for the

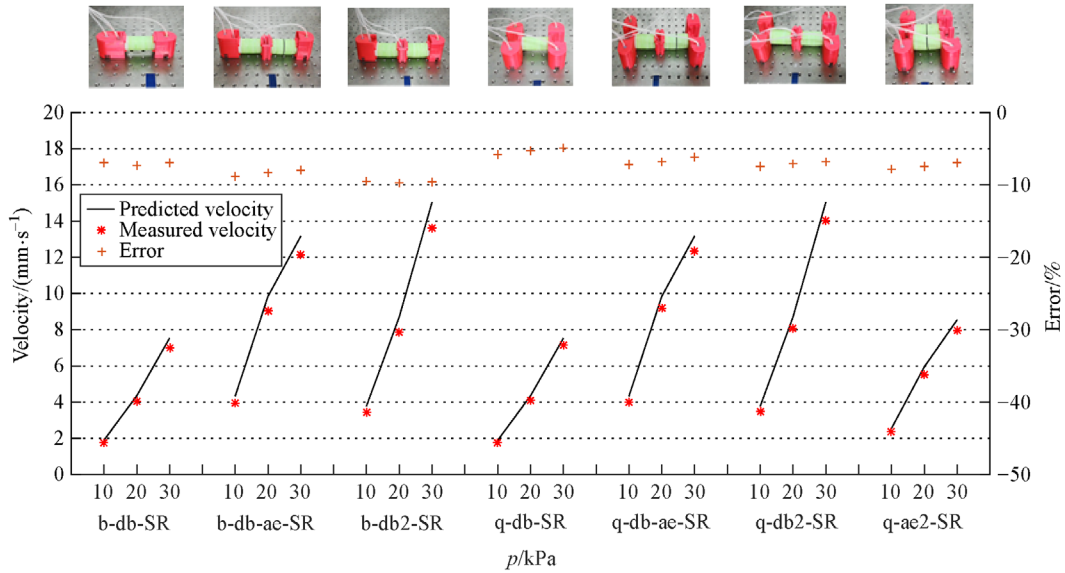


Fig. 16 Crawling velocities and errors of the robots.

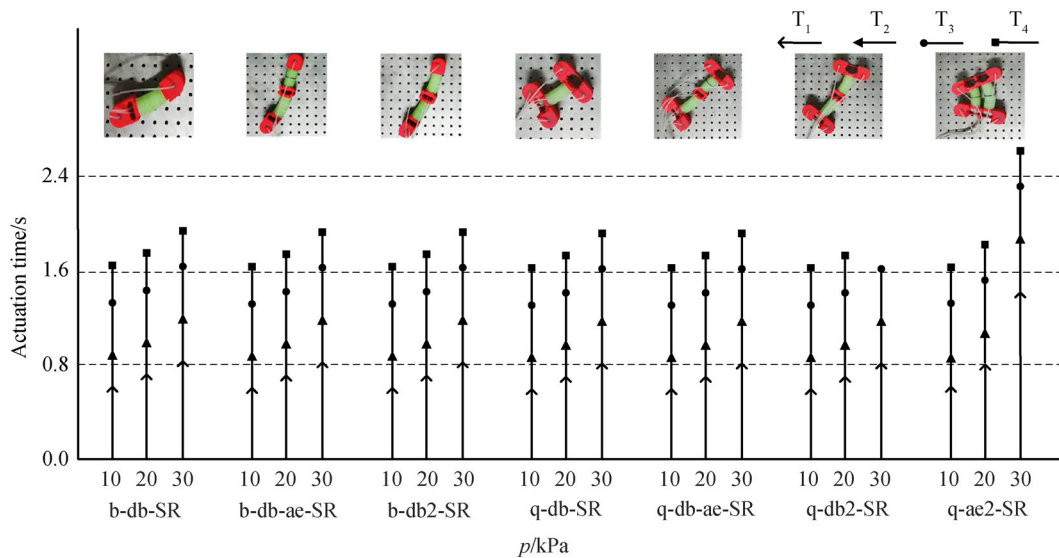


Fig. 17 Actuation time of turning for the different soft robots.

same robots at different pressures. This study adopts the simplified quasi-static model to characterize the deformation of SPAs and establishes a time-related model in a given period for crawling robots by using the response time of SPAs in the experiments. Building a dynamic model by introducing damping based on the rheological model of silicone and establishing the ordinary partial equation of the position may be more reliable. Furthermore, the influence of the environment and external force should be considered. In the future, closed-loop control will be used with integrated sensors to make the motions highly accurate.

Acknowledgements The authors gratefully acknowledge the reviewers' comments. This work was supported by the National Natural Science Foundation of China (Grant Nos. 52075180 and U1713207), the Science and Technology Program of Guangzhou (Grant No. 201904020020), and the Fundamental Research Funds for the Central Universities.

Open Access This article is licensed under a Creative Commons Attribution 4.0 International License, which permits use, sharing, adaptation, distribution, and reproduction in any medium or format, as long as you give appropriate credit to the original author(s) and the source, provide a link to the Creative Commons license, and indicate if changes were made.

The images or other third-party material in this article are included in the article's Creative Commons license unless indicated otherwise in a credit line to the material. If a material is not included in the article's Creative Commons

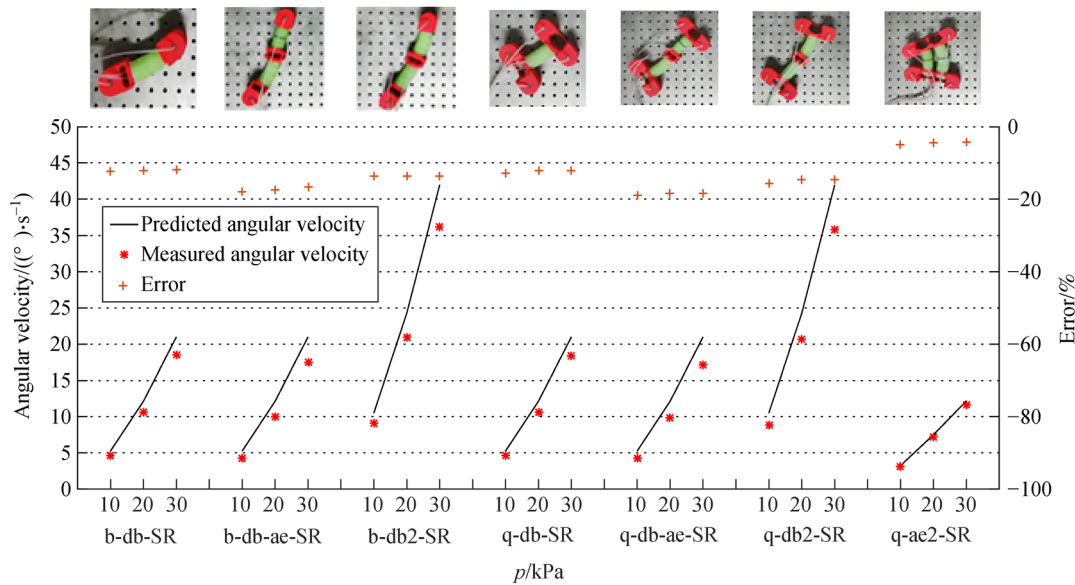


Fig. 18 Crawling angular velocities and errors of the robots.

license and your intended use is not permitted by statutory regulation or exceeds the permitted use, you will need to obtain permission directly from the copyright holder.

To view a copy of this license, visit <http://creativecommons.org/licenses/by/4.0/>.

References

- Wang N, Cui C, Guo H, et al. Advances in dielectric elastomer actuation technology. *Science China. Technological Sciences*, 2018, 61(10): 1512–1527
- Peng H, Yao H, Ding Q, et al. IPMC gripper static analysis based on finite element analysis. *Frontiers of Mechanical Engineering*, 2010, 5(2): 204–211
- Wang N, Guo H, Chen B, et al. Design of a rotary dielectric elastomer actuator using a topology optimization method based on pairs of curves. *Smart Materials and Structures*, 2018, 27(5): 055011
- Dong T, Zhang X, Liu T. Artificial muscles for wearable assistance and rehabilitation. *Frontiers of Information Technology & Electronic Engineering*, 2018, 19(11): 1303–1315
- Wang N, Guo H, Chen B, et al. Integrated design of actuation and mechanism of dielectric elastomers using topology optimization based on fat Bezier curves. *Soft Robotics*, 2019, 6(5): 644–656
- Wang N, Cui C, Chen B, et al. Design of translational and rotational bistable actuators based on dielectric elastomer. *Journal of Mechanisms and Robotics*, 2019, 11(4): 041011
- Bowen L, Springsteen K, Feldstein H, et al. Development and validation of a dynamic model of magneto-active elastomer actuation of the origami waterbomb base. *Journal of Mechanisms and Robotics*, 2015, 7(1): 011010
- Böse H, Rabindranath R, Ehrlich J. Soft magnetorheological elastomers as new actuators for valves. *Journal of Intelligent Material Systems and Structures*, 2012, 23(9): 989–994
- Metsch P, Kalina K A, Spieler C, et al. A numerical study on magnetostrictive phenomena in magnetorheological elastomers. *Computational Materials Science*, 2016, 124: 364–374
- Kim Y, Yuk H, Zhao R, et al. Printing ferromagnetic domains for untethered fast-transforming soft materials. *Nature*, 2018, 558(7709): 274–279
- Martinez R V, Fish C R, Chen X, et al. Elastomeric origami: programmable paperelastomer composites as pneumatic actuators. *Advanced Functional Materials*, 2012, 22(7): 1376–1384
- Terryn S, Brancart J, Lefeber D, et al. Self-healing soft pneumatic robots. *Science Robotics*, 2017, 2(9): eaan4268
- Rus D, Tolley M T. Design, fabrication and control of soft robots. *Nature*, 2015, 521(7553): 467–475
- Liang X, Cheong H, Chui C K, et al. A fabric-based wearable soft robotic limb. *Journal of Mechanisms and Robotics*, 2019, 11(3): 031003
- Situm Z, Trslc P. Ball and beam balancing mechanism actuated with pneumatic artificial muscles. *Journal of Mechanisms and Robotics*, 2018, 10(5): 055001
- Robertson M A, Sadeghi H, Florez J M, et al. Soft pneumatic actuator fascicles for high force and reliability. *Soft Robotics*, 2017, 4(1): 23–32
- Sun Y, Yap H K, Liang X, et al. Stiffness customization and patterning for property modulation of silicone-based soft pneumatic actuators. *Soft Robotics*, 2017, 4(3): 251–260
- Li H, Kawashima K, Tadano K, et al. Achieving haptic perception in forceps manipulator using pneumatic artificial muscle. *IEEE/ASME Transactions on Mechatronics*, 2013, 18(1): 74–85
- Okui M, Kobayashi M, Yamada Y, et al. Delta-type four-DOF force-feedback device composed of pneumatic artificial muscles and magnetorheological clutch and its application to lid opening. *Smart Materials and Structures*, 2019, 28(6): 064003
- Tondu B, Ippolito S, Guiochet J, et al. A seven-degrees-of-freedom robot-arm driven by pneumatic artificial muscles for humanoid

- robots. *International Journal of Robotics Research*, 2005, 24(4): 257–274
21. Ohta P, Valle L, King J, et al. Design of a lightweight soft robotic arm using pneumatic artificial muscles and inflatable sleeves. *Soft Robotics*, 2018, 5(2): 204–215
 22. Wang J, Liu Z, Fei Y. Design and testing of a soft rehabilitation glove integrating finger and wrist function. *Journal of Mechanisms and Robotics*, 2019, 11(1): 011015
 23. Hosoda K, Sakaguchi Y, Takayama H, et al. Pneumatic-driven jumping robot with anthropomorphic muscular skeleton structure. *Autonomous Robots*, 2010, 28(3): 307–316
 24. Shepherd R F, Ilievski F, Choi W, et al. Multigait soft robot. *Proceedings of the National Academy of Sciences of the United States of America*, 2011, 108(51): 20400–20403
 25. Satheeshbabu S, Krishnan G. Modeling the bending behavior of fiber-reinforced pneumatic actuators using a pseudo-rigid-body model. *Journal of Mechanisms and Robotics*, 2019, 11(3): 031011
 26. Qiao Q, Yuan J, Shi Y, et al. Structure, design, and modeling of an origami-inspired pneumatic solar tracking system for the NPU-phonesat. *Journal of Mechanisms and Robotics*, 2017, 9(1): 011004
 27. Felt W, David Remy C. A closed-form kinematic model for fiber-reinforced elastomeric enclosures. *Journal of Mechanisms and Robotics*, 2018, 10(1): 014501
 28. Connolly F, Polygerinos P, Walsh C J, et al. Mechanical programming of soft actuators by varying fiber angle. *Soft Robotics*, 2015, 2(1): 26–32
 29. Gorissen B, Chishiro T, Shimomura S, et al. Flexible pneumatic twisting actuators and their application to tilting micromirrors. *Sensors and Actuators. A, Physical*, 2014, 216: 426–431
 30. Mosadegh B, Polygerinos P, Keplinger C, et al. Pneumatic networks for soft robotics that actuate rapidly. *Advanced Functional Materials*, 2014, 24(15): 2163–2170
 31. Lee J, Kim W, Choi W, et al. Soft robotic blocks: Introducing SoBL, a fast-build modularized design block. *IEEE Robotics & Automation Magazine*, 2016, 23(3): 30–41
 32. Taylor A J, Montayre R, Zhao Z, et al. Modular force approximating soft robotic pneumatic actuator. *International Journal of Computer Assisted Radiology and Surgery*, 2018, 13(11): 1819–1827
 33. Eder M, Hisch F, Hauser H. Morphological computation-based control of a modular, pneumatically driven, soft robotic arm. *Advanced Robotics*, 2018, 32(7): 375–385
 34. Jiao Z, Ji C, Zou J, et al. Vacuum-powered soft pneumatic twisting actuators to empower new capabilities for soft robots. *Advanced Materials Technologies*, 2019, 4(1): 1800429
 35. Ning J, Ti C, Liu Y. Inchworm inspired pneumatic soft robot based on friction hysteresis. *Journal of Robotics and Automation*, 2017, 1(2): 54–63
 36. Calisti M, Picardi G, Laschi C. Fundamentals of soft robot locomotion. *Journal of the Royal Society, Interface*, 2017, 14(130): 20170101